Proceedings of ASME Turbo Expo 2026
TURBOMACHINERY TECHNICAL CONFERENCE AND EXPOSITION
June 15-19, 2026, Milan, Italy

GT2026-174810

DYNAMIC ANALYSIS OF REYNOLDS NUMBER EFFECTS ON TRAILING EDGE TRANSONIC VORTEX SHEDDING AND ITS IMPACT ON TURBINE BLADE AERODYNAMIC PERFORMANCE

Fernando Zigunov[1,†,*], Kenji Miki[2], Ali A. Ameri[2,3], Mark Wernet[2], Paul Giel[2,4,†,*]

[1]Syracuse University, Syracuse, NY
[2]NASA Glenn Research Center, Cleveland OH
[3]Ohio State University, Columbus, OH
[4]HX5 LLC, NASA Glenn Research Center, Cleveland, OH

ABSTRACT

Time-resolved, high-speed self-aligned focusing schlieren images were acquired in the NASA Glenn Research Center Transonic Turbine Blade Cascade facility to help understand the aerodynamic behavior of high-pressure, thick trailing edge turbine blades. The trailing edge thickness of 9% of axial chord tested represents simulated ceramic matrix composite fabrication constraints, which was verified previously to possess a high-loss flow regime at high inlet turbulence conditions over a narrow range of Reynolds numbers and at a fixed design exit Mach number of 0.74. Our high-speed images, which were acquired at 10 distinct Reynolds numbers, show a significant increase in energy from flow oscillations due to transonic vortex shedding at Reynolds numbers corresponding to the high loss conditions. For those conditions, strong acoustic waves turn into shock waves. Spectral Proper Orthogonal Decomposition of the high-speed images shows acoustic waves from trailing edge vortex shedding at all conditions, with increased spectral energy at the high-loss conditions and slightly increasing frequency (about 6%) as a function of Reynolds number. Analysis of potential feedback timing is performed using velocity fields from a previous LES simulation, considering different feedback mechanisms. Most noteworthy is the acoustic/shock-boundary layer interaction mechanism on the suction surface at the blade geometric throat, which likely plays an important role in realistic curved blade passages.

Keywords: Spectral POD, Transonic Vortex Shedding, Turbine, Trailing Edge

NOMENCLATURE

Flow conditions

$P_{t,1}$	Total pressure at inlet
$T_{t,1}$	Total temperature at inlet

Dimensionless numbers

Re	Reynolds number based on axial chord and isentropic exit flow conditions
Re_b	Baseline Reynolds number, $Re_b = 1.24 \times 10^6$
$M_{2,i}$	Outlet isentropic Mach number
St	Strouhal number, $St = f D_{TE}/u_{2,i}$
Zw	Zweifel Coefficient, $Zw = \frac{2S}{C_x}\beta_2(\tan\beta_1 - \tan\beta_2)$

Blade / cascade geometry

C_x	Axial chord length
D_{TE}	Trailing-edge thickness
S	Blade pitch
H	Blade span
$\beta_{1,des}$	Design inlet flow angle
$\bar{e}_2$	Integrated kinetic energy loss coefficient, $\bar{e}_2 = [(\frac{P_{t,1}}{\bar{P}_{t,2}})^{\frac{\gamma-1}{\gamma}} - 1]/[(\frac{P_{t,1}}{P_2})^{\frac{\gamma-1}{\gamma}} - 1]$

Mathematical quantities

f	Frequency
Λ	SPOD eigenvalue matrix
λ	SPOD eigenvalue matrix element
Ψ	SPOD eigenvector matrix

Superscripts and subscripts

b	Baseline condition
i	Isentropic value from pressure ratio $\frac{P_{t,1}}{P_2}$
1	Cascade inlet
2	Cascade exit
t	Total condition

1. INTRODUCTION

New developments in ceramic matrix composites (CMC's) that can withstand very high temperatures have renewed interest in studying high-pressure turbine blades with thick trailing edges due to the CMC material being laid in plies during the manufacturing of the blades [1]. The individual layers have a minimum bending radius, which added to the thickness of all layers results in a minimum radius at the trailing edge location. By operating

†Joint first authors
*Corresponding author: paul.w.giel@nasa.gov

at higher temperatures, higher cycle efficiency can be achieved leading to higher thrust-to-weight ratios. Because CMC turbine blades would require stricter geometric constraints with larger minimum radii of curvature, it is crucial to assess the effect of the increased curvature that will produce a blunter trailing edge, leading to vigorous vortex shedding that is related to lower overall efficiency [2].

Within this context, Giel et al. [3] reported on a study of the aerodynamic performance of simulated CMC blades with trailing edge (TE) thicknesses of 5%, 7%, and 9% of axial chord, C_x. All tests were performed at the design exit isentropic Mach number, $M_{2,i} = 0.742$ and used a pneumatic 5-hole probe to measure the blade wakes. They found that for one particular combination of TE thickness, inlet turbulence level, and Reynolds number, the aerodynamic loss was significantly higher (~44%) than the anticipated power law regression value. This case was originally considered to be an anomaly but after acquiring data at additional Reynolds numbers [4], it was considered to be more intriguing. In thick turbine blade trailing edges, a phenomenon called transonic vortex shedding (TVS) may occur if the Von Karman vortex street produced at the trailing edges causes temporary flow accelerations beyond the sonic speed, producing shock waves that increase the total loss and therefore reduce the efficiency of the turbine cascade [5].

The more detailed Large Eddy Simulations (LES) by Miki et al. [4] followed on the work by Giel et al. [3] trying to pin down the mechanisms for this excessive loss at a specific Reynolds number. Their observations pointed to the presence of a shock train (a series of evenly-spaced shock waves) traveling upstream that was significantly enhanced within the anomalous Reynolds number ($Re/Re_b = 1.00$), which they conjectured to interact with the suction-side boundary layer (a shock-boundary layer interaction, or SBLI). SBLI's are known to facilitate boundary layer separation and produce increased unsteadiness [6]; potentially enhancing the trailing edge vortex shedding mechanism if the excitation causes the formation of an unsteady separation bubble that can provide a source of large disturbances.

Increased loss at a narrow band of conditions was observed by Melzer and Pullan [5] for a single straight blade in a channel with the effect worsening for thicker trailing edges. By varying the Mach number, they observed certain values of $M_{2,i}$ produced peak loss and some intermediate values produced much lower loss. Their schlieren images for the single blade case point to a resonance mechanism, where the transonic vortex shedding at the trailing edge produces a shock train that, with the correct conditions, propagates through the free stream, reflects from the wall of the test section, and returns with the correct phase to interfere constructively at the maximum loss conditions or destructively at the minimum loss conditions. However, their observations on a turbine cascade when varying the Reynolds number instead pointed to a single step in loss, where the loss simply increases greatly after a given Reynolds number when the Mach number is maintained constant. This observation was further corroborated in their follow-up publications [7, 8], but it is notably different from the behavior observed by Giel et al. [3], where the loss returned to a lower value as the Reynolds number continued to be increased. Rossiter [8] also noted the important role that

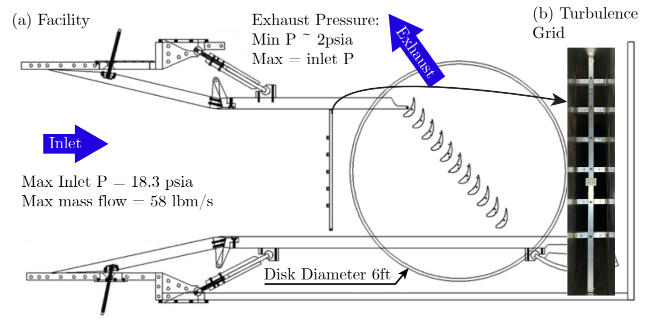

FIGURE 1: TRANSONIC TURBINE CASCADE FACILITY AT NASA GRC.

the boundary layer state plays in the increased loss regime, with the transition to turbulence and its associated reduction in shape factor being detectable as the TVS regime starts.

Several pathways appear to be viable for enhanced transonic vortex shedding that could cause a turbine blade cascade design to yield significantly lower performance than expected. The boundary layer state seems to be an important factor, as it triggers a transition of vortex shedding regime that is similar to what is observed in simpler bluff bodies such as the cylinder in cross-flow. As proposed by Rossiter et al. [7], a laminar trailing edge shear layer would be more stable and thus less prone to producing sufficiently strong vortex shedding to trigger TVS. However, the potential role of resonance and acoustic or shock wave interaction with the boundary layer being the root cause of the transition to turbulence could be an important link that may improve the explanation of why this switch is observed by Giel et al. [3] with increased intensity for a narrow range of Reynolds numbers. Following the insight provided by the LES simulations of Miki et al. [4], which covered two Reynolds numbers, we isolate the Reynolds number effect in this work through a detailed parameter scan of time-resolved, high-speed Self Aligning Focusing schlieren images acquired at 10 Reynolds numbers and advanced processing of the images using Spectral Proper Orthogonal Decomposition (POD) to further our understanding of the anomaly observed.

2. MATERIALS AND METHODS

2.1. Cascade Facility

The images presented in this work are based on tests at the NASA Glenn Transonic Turbine Cascade Facility shown in Figure 1. The turbine cascade model is comprised of ten passages built from eleven two-dimensional extrusions of the CMC-9 blade profile, which has a trailing edge thickness D_{TE} equal to 9% of the axial chord of the blade. The remaining dimensions and parameters of this blade are provided in Table 1.

The inlet of the facility is supplied by NASA GRC's 40 psig combustion air system. The air is filtered, dried, brought to ambient temperature and throttled down to a maximum of 18.3 psia before it enters the facility. The air then goes through a series of flow conditioners and contraction sections before it meets the blade cascade, where it is extracted through an exhaust header at 2 psia. Inlet and outlet valves were controlled to set and maintain

Parameter	Value
Axial chord C_x	5.119"
Blade Pitch S	5.119"
Blade Span H	6.000"
Throat Gage Dimension	2.097"
Throat/C_x	0.41
Design Inlet Flow Angle $\beta_{1,des}$	29.7°
Test Inlet Flow Angle β_1	38.8°
Trailing Edge Metal Angle	−60.9°
Zweifel Coefficient Zw at β_1	1.23
Leading Edge Diameter	0.885"
Trailing Edge Diameter	0.460"
D_{TE}/C_x	9.0%

TABLE 1: CMC-9 BLADE PARAMETERS.

cascade pressure level and pressure ratio, setting the Reynolds and Mach numbers independently to the desired conditions.

Figure 1 shows the blade cascade section, which is mounted on a disk that can be rotated to achieve the desired inlet angle β_1, where the contraction is adjusted to maintain a straight channel inlet condition at the blades. The tests presented herein were conducted at an inlet flow angle $\beta_1 = 38.8°$. The blade trailing edge thickness, $D_{TE}/C_x = 0.09$, is chosen for further examination as it was observed in our earlier measurements [3] that it produced the anomalous loss at a certain Reynolds number value ($Re_{C_x} = 1.24 \times 10^6$ or $Re/Re_b = 1.00$) that could be related to the TVS phenomenon. The anomaly, however, was most evident only at the higher inlet turbulence case, $Tu_{in} \approx 13\%$, so only this condition is examined here. Further details on the blade loading, inlet boundary layer state, and inlet turbulence are detailed in previous publications [3, 9–12].

The turbulence grid used to produce $Tu_{in} \approx 13\%$ was fabricated from 1" square tubes and used upstream blowing from 1/8" diameter holes on 1/2" centers on the vertical and horizontal bars. Air was supplied through the sidewalls to both ends of the horizontal bars, which in turn supplied the vertical bar through ports at the bar junctions. The blowing rate was adjusted to about 1.1% of the primary cascade flow to successfully minimize the mean flow wakes from the bars. A view of the grid looking upstream is shown in Figure 1 (b). The grid is located approximately $7.4C_x$ upstream of the leading edge of the primary measurement blade #5. The vertical bar is centered on the 6" span, and the six horizontal bars are centered 6" apart, resulting in an open area of about 63%. Inlet turbulence survey measurements are reported in Thurman et al. [12]. At the primary measurement passage, the inlet turbulence was 13% and varied by ±2.6% in the pitchwise direction because of the difference in streamwise distances between the grid and the cascade face. The integral length scale was approximately $0.1C_x$ with little pitchwise variation noted.

As shown in Figure 1, no tailboards are used in the facility. Instead, flow periodicity is obtained in the center three passages by the high blade count and by the adjustability of the upper- and lowermost end passage flow areas. The blade loading data acquired from the three primary measurement blades and the wake survey data acquired over three blade pitches as presented in Giel et al. [3] show excellent periodicity.

Re/Re_b	View #	$M_{2,i}$	$P_{t,1}$ (psia)	$T_{t,1}$ (°F)
0.25	1	0.743	2.708	81.20
0.50	1	0.742	5.386	79.81
0.57	1	0.743	6.066	74.53
0.66	1	0.743	7.019	75.17
0.76	1	0.741	8.113	75.53
0.87	1	0.741	9.280	75.90
1.00	1	0.742	10.767	80.07
1.14	1	0.742	12.186	76.41
1.31	1	0.741	14.015	77.65
1.50	1	0.741	16.240	80.54
0.25	2	0.744	2.728	86.88
0.50	2	0.742	5.468	87.48
0.57	2	0.742	6.171	82.58
0.66	2	0.742	7.182	82.89
0.76	2	0.742	7.694	81.66
0.87	2	0.741	9.458	82.13
1.00	2	0.740	11.034	89.59
1.14	2	0.741	12.340	82.96
1.31	2	0.743	13.338	84.00
1.50	2	0.741	15.298	85.06

TABLE 2: TEST CONDITIONS FOR EACH RUN.

2.2. Self-Aligned Focusing Schlieren

To acquire the images discussed in this work, a time-resolved Self-Aligning Focusing Schlieren (SAFS) system, developed initially by Bathel and Weisberger [13] and further described in [14], was employed. One notable difference in our SAFS system is that we employ wire-grid linear polarizers and instead of a polarization beam splitting cube, a 3^{rd} wire grid polarizer is used to polarize and turn the light source beam down the axis of the SAFS system. The advantage of the SAFS system is its portability, as the optical system can be easily moved across facilities without the necessity for highly-rigid mirror mounts or their alignment, being ideal to service the multiple facilities at GRC. The SAFS system was configured to provide approximately a 4.5" wide field of view. Two views were considered, as displayed in Figure 2, where View 1 focuses on the flow features downstream of the trailing edge and View 2 focuses on the suction surface boundary layer. A Photron SA-Z camera, equipped with 128GB of RAM and sampling at 20,000 fps, captured the images formed in the SAFS optical train through a relay lens at a resolution of 1024×1024 px for a total record duration of approximately 4.4 seconds. For the images displayed in this work, the focal plane of the SAFS system is placed in the center plane of the test section.

The focusing schlieren optical train works by projecting the 20 line pairs/mm Ronchi Ruling onto the schlieren object by using the Cavilux laser as a light source exposing the schlieren object for a 30 nanosecond pulse duration. The Cavilux laser light passes through a vertical linear polarizer and is reflected through the plate beam splitter (another vertical polarizer) into the flow domain. The light travels through the Ronchi ruling and through a glass/quartz Wollaston prism with a 7.5 arc-minute deviation angle towards the field lens, which focuses the image of the Ronchi ruling onto the retroreflective background at the opposite side of the cascade. The quarter wave plate ($\lambda/4$) turns the linearly polarized light into right-handed circularly polarized

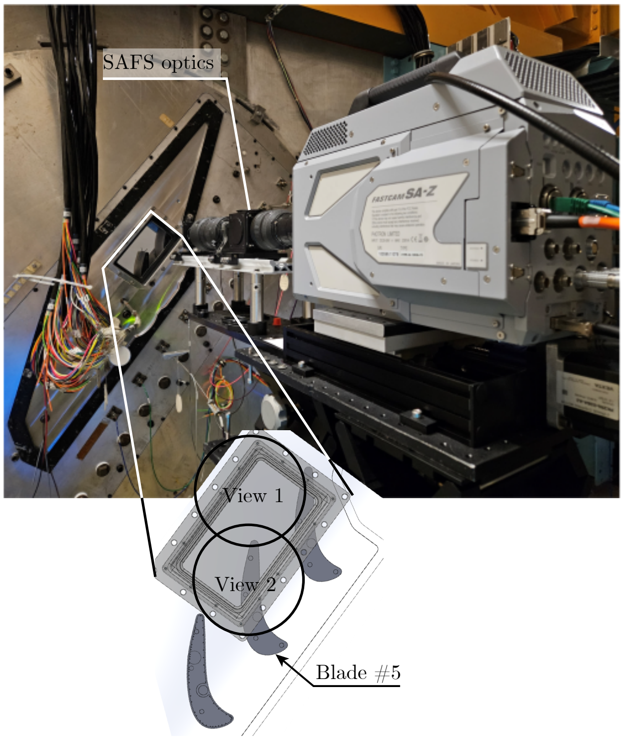

FIGURE 2: PHOTOGRAPH OF THE SELF-ALIGNED FOCUSING SCHLIEREN SETUP AND ARRANGEMENT OF THE VIEWS TAKEN DURING THIS CAMPAIGN.

light. When the light passes through the schlieren object and is reflected back from the retroreflective background, its circular polarization handedness is flipped to left-handed circularly polarized light such that when it passes through the quarter wave plate again it will be rotated into horizontal linearly polarized light, which is perpendicular to the outgoing light. Only horizontally polarized light is permitted to enter the camera through the horizontal polarizer and the relay lens, providing discrimination from the outgoing vertical linearly polarized light. The Wollaston prism is then able to provide a small angular shift to the oncoming beam, which is then cut off by the same Ronchi ruling without requiring any alignment as the grid automatically has a matching conjugate plane at its mirror image by construction. In our SAFS system, the field lens image focal plane sits inside the optical train and therefore a relay lens needs to be placed between the camera sensor and the beam splitter to properly image the cascade flow. A relay lens and a set of extension tubes were required as the conjugate plane to the schlieren object was located in front of the Ronchi ruling.

The Ronchi ruling is placed with the lines aligned vertically with respect to the ground, meaning the density gradient direction measured is such that the shear layers of the blade trailing edges are most highlighted.

2.3. LES simulations

The analysis on wave timing performed in the discussion presented herein utilized the time-averaged results from the LES simulations performed by Miki et al. [4]. We here leverage only the mean field from the $Re/Re_b = 1.00$ case, while acknowledging that slight variations in the flow field between the different Reynolds number conditions may be responsible for the changes we observe in our experiments.

The LES simulations by Miki et al. [4] were accomplished with the in-house code Glenn-HT [15], using structured multi-block grids. Given the high Reynolds number of this application, the mesh required for accurate LES was very dense, utilizing a total of 290 million grid elements to resolve the $0.1C_x$ span of the computational domain. Further details on the simulation setup, results and boundary conditions can be found in the original publication [4].

3. FLOW STATES

First, we present the original images captured with minimal processing in this section. Figure 3 shows the mean-subtracted images acquired from the two views (each experiment conducted independently), arranged to their approximate locations in the blade. The images are tiled (there are two copies of each view) to clarify the wraparound connection points across views, as the standalone images can be difficult to understand outside of the context of the blade arrangement. The images presented are instantaneous snapshots from experiments where the Reynolds number is varied but the Mach number of the exit is maintained constant at $M_{2,i} = 0.742$ within the facility capabilities. A subset of the dataset acquired is presented to facilitate the discussion and interpretation.

It is immediately evident in Figure 3 that the first two Reynolds numbers present only strong features at the wake of the blade, without significant density gradients detected in between the blades. As the Reynolds number is increased to $Re/Re_b = 0.66$, weak waves start appearing in the images, and at $Re/Re_b = 0.76$ the waves develop into clear shock waves. At $Re/Re_b = 1.00$ and $Re/Re_b = 0.87$ (not shown), the shock production is most consistent every shedding cycle throughout the acquired footage. This is in contrast with the higher $Re/Re_b = 1.50$, where a very low frequency intermittency/modulation is observed; translating to sections in the footage where the shockwave production strength alternatively switches between quiet and loud moments.

To present evidence of this intermittent regime, we provide one snapshot at the quiet ("no shocks") and one snapshot at the loud ("shocks") cycle under $Re/Re_b = 1.50$ in Figure 3. Further evidence of this behavior is clear from watching the time-resolved shadowgraph video. In printed format, it is difficult to convey this information; so we provide a space-time wave diagram showing a slice of the time-resolved schlieren image along a line away from the pressure wall as shown in Figure 3, where the signal and intermittency is most clearly observed in printed format. As can be seen in Figure 4, the signal for $Re/Re_b = 0.50$ presents only a faint signature related to the upstream-propagating acoustic waves observed. For the most vigorous shock-forming cases $Re/Re_b = 0.87$ and 1.00, we observe consistent shock formation throughout the sample time provided, as witnessed by the diagonal stripes; each indicating the path of an upstream-propagating shock wave originated at the trailing edge by the vortex shedding process. However, at $Re/Re_b = 1.50$, we clearly observe the

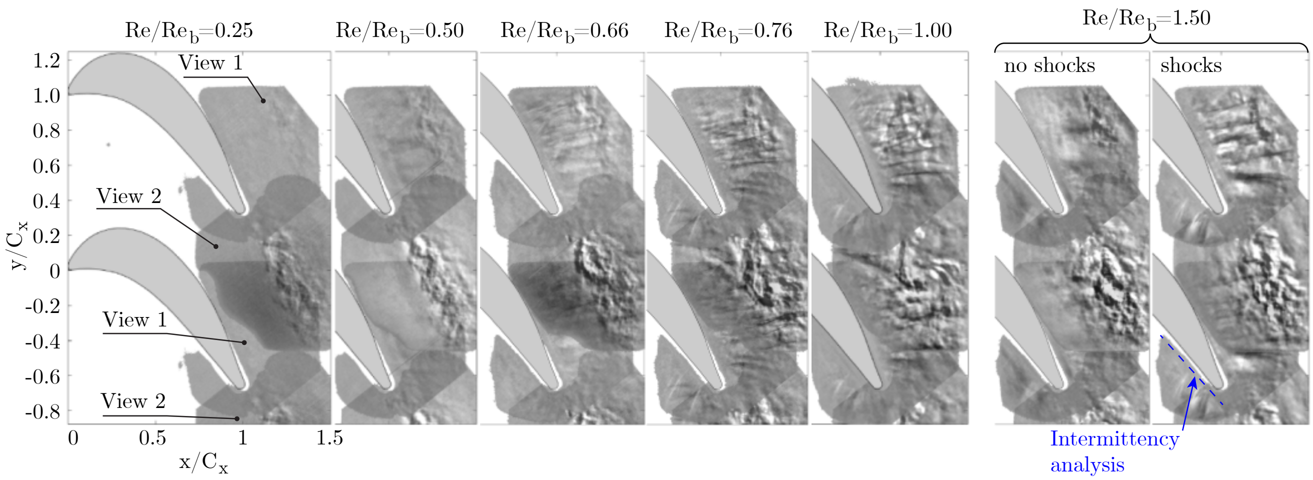

FIGURE 3: MOSAIC COMBINING THE RAW SAFS IMAGES FROM THE TWO VIEWS ACQUIRED IN THE BLADE COORDINATE FRAME AT $M_{2,i}$ = 0.74 FOR SELECTED REYNOLDS NUMBERS. COLOR SCALES IN ALL IMAGES ARE MATCHING TO ENABLE COMPARISON OF RELATIVE FEATURE STRENGTHS.

intermittent switching between shock formation (at $t < 4$ ms) and shock absence ($t > 5$ ms). This figure only presents one cycle of this intermittency behavior in order to have appropriate magnification of the features to highlight it, but the alternation between "shocks" and "no shocks" zones persists throughout the entire footage acquired ($\sim$ 4.3 s). One could also argue some modulation of the shock strength may also be present in the Re/Re_b = 1.00 case, though to a lesser extent. We did not rule out, however, that this could be related to the dynamics of other components of the facility, as the modulation frequency appears to be too slow at a first glance ($St_{Cx} \sim 0.045$) to be related to the fluid phenomena in the blade passage, although low-frequency oscillations have been observed in early works in another facility [16] and were ascribed to coupling between the cascade flow and unsteadiness in the free shear layer downstream of the cascade.

To put this intermittency effect into context with the loss measurements we observe for this blade cascade, we provide Figure 5 annotated with the observations from our high-speed footage. There appears to be three regimes in our footage: (1) A no-shock regime (region in blue) where only acoustic waves are seen; (2) a transonic vortex shedding regime (region in red) where the losses are significantly higher, peaking at approximately Re/Re_b = 0.87. Finally, a later regime at higher Reynolds numbers is observed (3) where the transonic vortex shedding is intermittent and still produces shock wave trains momentarily as bursts. This regime, as we observe in our footage, alternates between periods of shock production (high-loss) and no shocks (low-loss), and we conjecture their averaged effect asymptotes to a low value of averaged loss coefficient as the duty cycle of the active shock production period decreases. Note the transition between regimes (1) and (2) is smooth, and the acoustic waves intensify in strength until they become shock waves.

4. SPECTRAL POD ANALYSIS

From the analysis of the raw schlieren images, we observed that there is a clear effect of Reynolds number on the presence of shock waves, which seems to impact the overall loss of the

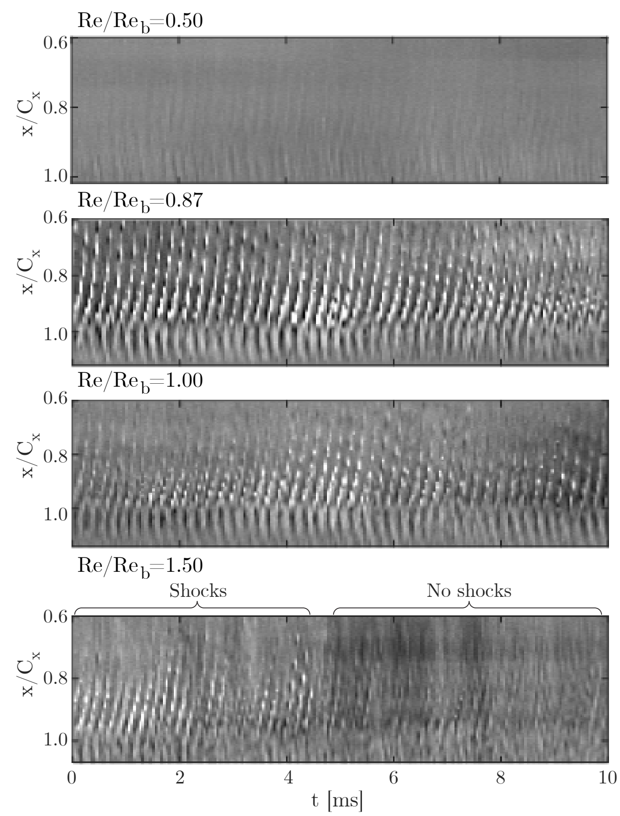

FIGURE 4: SPACE-TIME DIAGRAMS ON PRESSURE SIDE SHOWING UPSTREAM-PROPAGATING SHOCKS FOR VARIOUS REYNOLDS NUMBERS.

blades as observed in [3] detailing the information gleaned from the wake pressure measurements. Here we extract further insight from the high-speed images acquired to understand the potential causes for the transonic vortex shedding only at a certain range of Reynolds numbers.

The high-speed footage contains what effectively amounts to

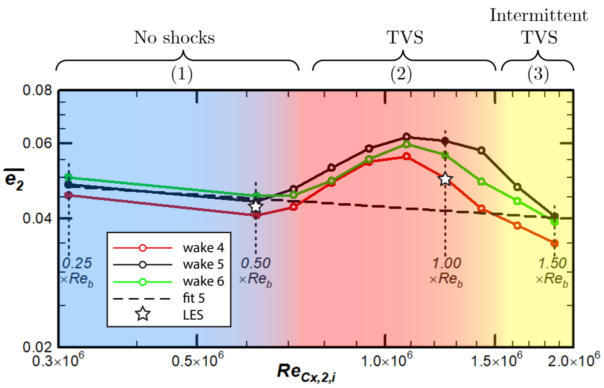

FIGURE 5: INTERMITTENCY IN CONTEXT WITH OBSERVED INTEGRATED WAKE LOSSES $\bar{e}_2$ FROM PRESSURE SURVEY AND LES SIMULATIONS FROM [4].

a large number of simultaneously-acquired high-bandwidth sensors with a Nyquist frequency equal to half the frame rate. Thus, a spectral analysis on the signals from each pixel should reveal the frequency content associated with the dynamics of the underlying phenomenon causing the pixel intensity to vary. As the images acquired have a resolution of 1024×1024 px, there are approximately 1 million simultaneously acquired signals from which information can be gleaned. The Spectral POD analysis technique, although popularized by Towne et al. [17] through their open-source code base, was first formally introduced by Sieber et al. [18] and was effectively used to analyze simultaneously-acquired time-resolved sensor data as early as 1997 by Arndt et al. [19] and Delville et al. [20]. Here we use the formulation defined in [17], where an eigenvalue decomposition of the cross-spectral density matrix is performed for each frequency to find the most energetic/relevant single-frequency phase relationships across different regions in the image. As outlined in [21], this process is akin to performing a Welch averaged estimate of the eigenvectors and eigenvalues of the cross-spectral density matrix based on the data. We point the unfamiliar reader to [21], Section 3, for a brief but effective discussion about the details of the processing technique.

By applying Spectral POD to the SAFS images acquired in this experiment, two groups of information are extracted. First, a group of eigenvalue spectra, Λ, shows the relative energy in the fluctuations contained in the underlying images is obtained for each frequency and mode. The spectra can be plotted as regular frequency-amplitude spectra and interpreted accordingly by identification of peak amplitudes that can be related to important cyclical phenomena in the flow, or broadly-distributed amplitudes that are related to broadband noise or turbulence. Second, a group of eigenvectors, Ψ, is calculated from the images, each of which being a complex-phase diagram corresponding to a specific frequency and mode number. The most energetic modes will contain the first-order information and are generally sufficient to glean insight about the important fluid dynamics present in the underlying images. Upon examination of the convergence of SPOD for our datasets, we observe that convergence of the spectra and mode shapes happens quickly and that the results are independent of

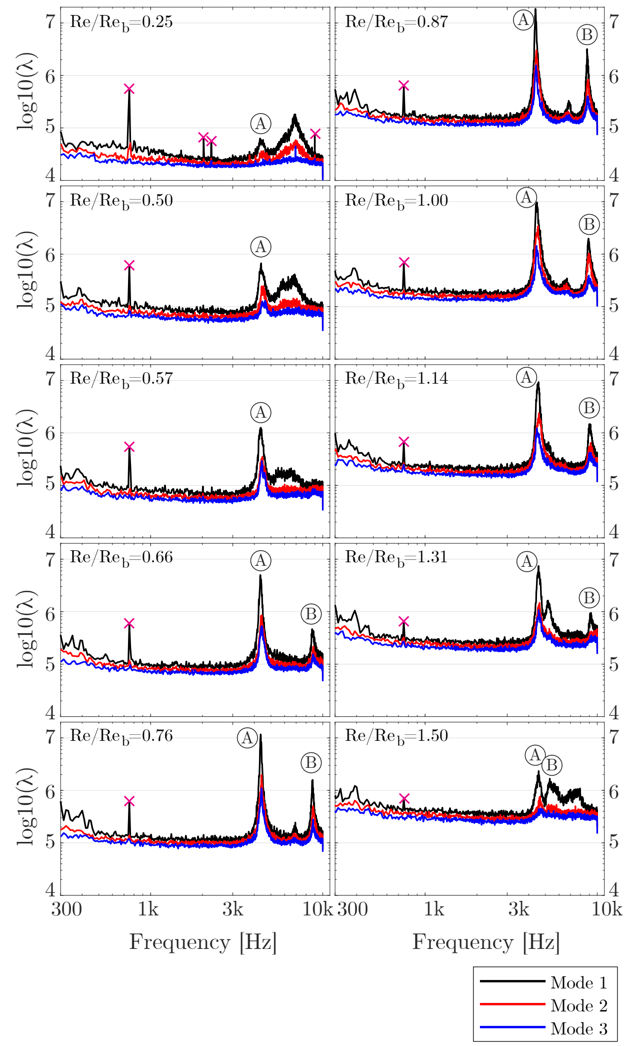

FIGURE 6: SPOD SPECTRA FOR THE THREE MOST ENERGETIC MODES FOR ALL REYNOLDS NUMBERS TESTED (VIEW 1). PEAKS MARKED WITH A PURPLE × ARE CAMERA ARTIFACTS. PEAKS MARKED WITH (A) AND (B) ARE RELATED TO VORTEX SHEDDING DYNAMICS.

the processing parameters chosen. Although we present results with 124 overlapping blocks of 2048 images with 75% overlap, we found the modes and spectra are well-converged even for as few as 12 blocks.

With the interpretation details related to the SPOD technique discussed, we now refer the reader's attention to Figure 6, where the eigenvalue spectra for the first three modes of the Spectral POD eigenspectrum are provided for all Reynolds numbers tested. Each line corresponds to a magnitude-ranked element of the diagonal of the eigenvalue matrix Λ, indicating the relative amount of energy contained at each frequency for the particular mode rank corresponding to each line. Here, we only present the first three modes, as the majority of the low-order dynamics can be gleaned by only the first SPOD mode. As can be noted in Figure 6, all cases display a generally flat spectrum with a sharp peak at a very low frequency ($\sim$ 700 Hz) and a group of one to three broader peaks at a high frequency ranging between $\sim$ 4 and

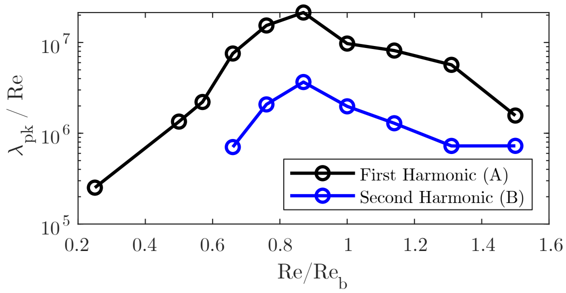

FIGURE 7: INTENSITY OF MODE 1 PEAK FOR THE FIRST AND SECOND HARMONICS (VIEW 1) AS A FUNCTION OF REYNOLDS NUMBER. (A) AND (B) REFER TO PEAKS INDICATED IN FIGURE 6.

$\sim$ 9 kHz. The low-frequency sharp peak, along with the other peaks marked with an $\times$ are not relevant to the fluid dynamics, and represent spatiotemporally-correlated camera artifacts that are believed to be related to the camera sensor and electronics architecture and the camera noise floor (these peaks will not be discussed further in this manuscript).

The higher-frequency peaks in Figure 6 are, on the other hand, corresponding to interesting fluid phenomena and will be explored further in this section. Note the vertical scale (eigenvalue λ) is logarithmic, and therefore the peaks have significantly different strengths for each Reynolds number. Examining the peaks at the lower Reynolds numbers $Re/Re_b = 0.25$ and 0.50, they are widest and contain the least energy in the set, indicating wideband, less coherent phenomena. As the Reynolds number is increased past $Re/Re_b = 0.57$ the peaks become sharper and taller, and a second harmonic peak marked with (B) appears. However, as the Reynolds number is further increased beyond $Re/Re_b = 0.87$, the amplitude diminishes and the peak loses sharpness until at $Re/Re_b = 1.50$ several neighboring non-harmonic peaks at similar amplitude seem to spread the energy to a wider band.

This behavior points to a sort of resonant feedback mechanism, which is best highlighted when the height of the peaks is plotted as a function of Reynolds number, as shown in Figure 7. As can be observed, the peak height λ_{pk} increases with Reynolds number until the peak value at $Re/Re_b = 0.87$, subsequently decreasing as the Reynolds number continues increasing. Here we present the peak intensity λ_{pk} normalized by the Reynolds number (λ_{pk}/Re), as the schlieren intensity signal is proportional to the density gradient, which is itself proportional to pressure and thus to Reynolds number as the method utilized to vary the Reynolds number in this experiment is by varying the density of the air passing through the cascade. Even after compensating for this effect there is a clear formation of a maximum peak at $Re/Re_b = 0.87$ that is about 100$\times$ taller than the first harmonic intensity observed in the lowest Reynolds number case $Re/Re_b = 0.25$. The behavior is clearly distinguished in both harmonics (the second harmonic is not detected accurately for the lower Reynolds number cases and is omitted). After finding that the tallest peak occurred at $Re/Re_b = 0.87$ and not $Re/Re_b = 1.00$, we went back to our pressure loss data and observed that the loss is indeed maximal at $Re/Re_b = 0.87$ (see Figure 5); thereby further supporting the findings presented herein.

Before we discuss the possible sources of this resonance mechanism, it is worth looking at the SPOD eigenvectors, or 'mode shapes', which are comprised of complex-valued single-frequency pictures of the most coherent dynamics observed in the images. These mode shapes are displayed on Figure 8 for the first harmonic peak (A) in Figure 6, detected at approximately 4.3 kHz, and on Figure 9 for the second peak (B) detected at frequencies between 6 and 9 kHz. The figures display the wave behavior that is highlighted at the two frequencies, stemming from the most significant cross-correlations of the time series across different pixel spatial locations. Because the modes from SPOD are complex-valued, we present the real value of a single phase (zero degrees) on a centered red-white-blue color scale to represent the relative phases of the positive versus negative fluctuations for a frozen snapshot in time. Since the images are comprised of complex numbers, it is possible to advance the time for the mode at that particular frequency by multiplying the entire image by a phase value, $e^{2\pi i f t}$, enabling the detection of the wave propagation direction. The propagation direction gleaned from this process is displayed as arrows in Figures 8 and 9.

As is immediately noticed in Figure 8, all cases with the exception of $Re/Re_b = 0.25$ display a very similar set of waves with a downstream-propagating vortex street related to the trailing edge vortex shedding and an upstream-propagating acoustic/shock wave train emanating from the trailing edge of the blade and propagating both on the pressure and suction sides of the blade. In fact, even the $Re/Re_b = 0.25$ also presents the same acoustic wave image if the color scale is stretched further (not shown for consistency of the color scales presented).

Note the waves have similar intensity in Figure 8 because SPOD automatically normalizes the modes to be of unitary norm (or, in other words, the variance of all pixels in the image is normalized to be one). Therefore, one must interpret the images in Figures 8 and 9 as an intensity map that must be multiplied by the corresponding eigenvalue (from the peaks in Figure 7) to recover the original images. Thus, the wave intensities vary greatly across Reynolds numbers, but their shape and topology remains consistent; pointing us towards the same phenomenology that persists across Reynolds numbers and in certain conditions causes amplification of the waves that results in production of shocks. The region of high-loss TVS (zone 2 in Figure 5) is highly correlated by the presence of strong wave production as gleaned by the peak eigenvalue at $Re/Re_b = 0.87$ in Figure 7 and the presence of waves in the eigenvectors in Figures 8 and 9 at the range of Reynolds numbers $0.66 < Re/Re_b < 1.31$.

We observe the second harmonic shape in Figure 9, corresponding to the (B) peaks in Figure 6, displays the same general shapes with twice the spatial frequency, however the differences across Reynolds numbers are more notable: The range of Reynolds numbers from $0.66 < Re/Re_b < 1.31$ display upstream-propagating acoustics with similar strength as the trailing edge vortex shedding and their frequency is twice the fundamental frequency shown in Figure 8, whereas the cases with Reynolds numbers outside that range display weakened or no detectable acoustics at the second peak frequency, and the value

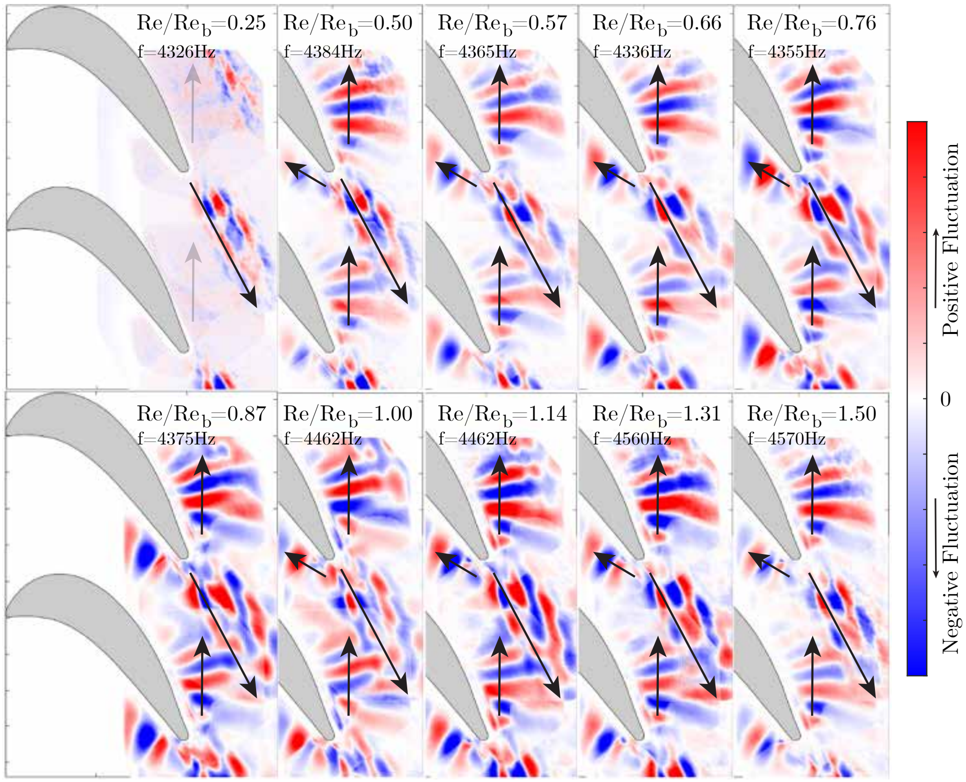

FIGURE 8: SPOD MODE #1 SHAPES (AT APPROXIMATELY 4.3 KHZ) RELATED TO THE FIRST HARMONIC PEAK IN FIGURE 6. ARROWS INDICATE DIRECTION OF WAVE PROPAGATION. WAVE PHASES MAY BE OUT-OF-SYNC ACROSS VIEWS 1 & 2.

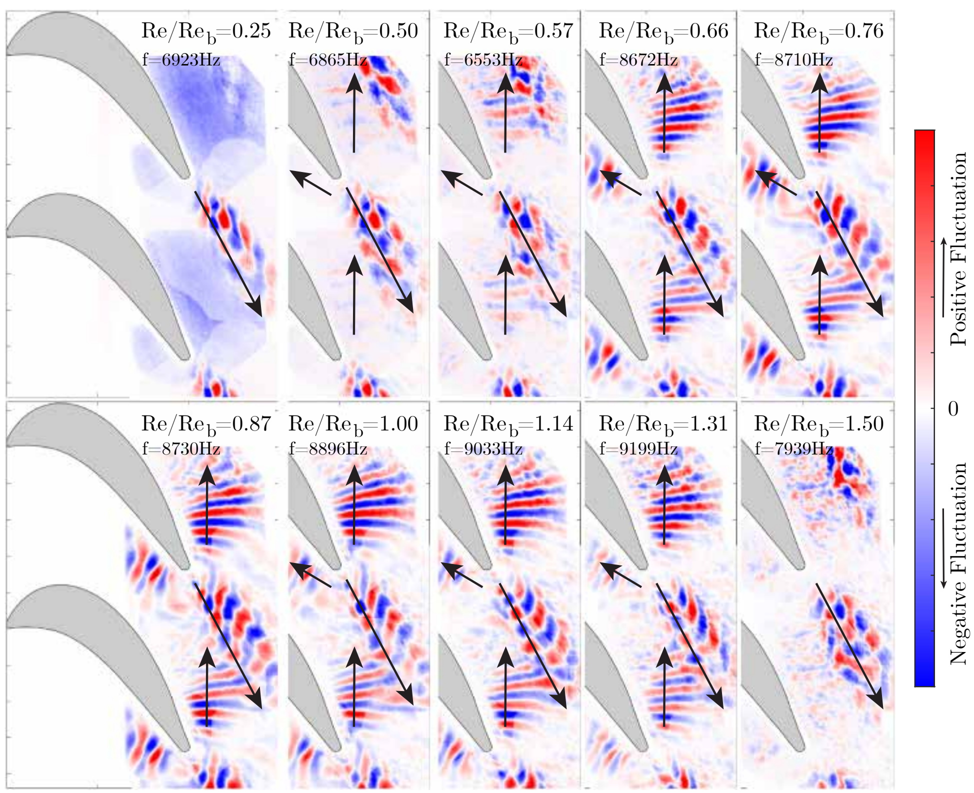

FIGURE 9: SPOD MODE #1 MODE SHAPES (BETWEEN 6-9 KHZ) RELATED TO THE SECOND PEAK IN FIGURE 6. ARROWS INDICATE DIRECTION OF WAVE PROPAGATION. WAVE PHASES MAY BE OUT-OF-SYNC ACROSS VIEWS 1 & 2.

of the second peak frequency is no longer twice the fundamental shedding. The case Re/Re_b = 1.50 not displaying waves in the SPOD is consistent with the lack of a clear SPOD peak in that region, and may be related to the intermittency phenomenon discussed in Section 3. This would indicate that the fundamental acoustic wave amplitude at ~ 4 kHz only generates a second harmonic once its amplitude is sufficiently large to trigger a non-linear wave steepening. As the shedding intensity becomes increasingly stronger, the acoustic wave produced at the fundamental frequency becomes more powerful, eventually reaching a level where non-linear acoustics is possible. This stronger acoustic steepens, forming a N-wave [22] that appears in our images as upstream-propagating shocks. The wave steepening process is facilitated by the fact the wave propagates against a high-speed stream, greatly increasing its wavenumber for a given frequency. The question that remains, evidently, is: What causes the trailing edge vortex shedding to have different amplitudes at what apparently seems to be the same frequency for only a certain range of Reynolds numbers?

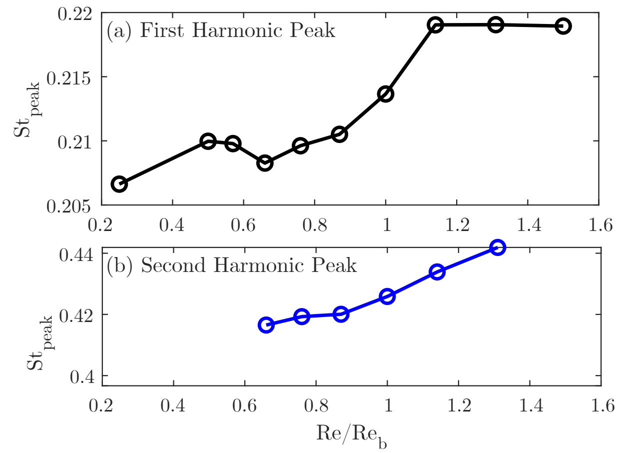

FIGURE 10: SPOD PEAK STROUHAL NUMBER $St = fD_{TE}/u_{2,i}$ AS A FUNCTION OF REYNOLDS NUMBER FOR THE (A) FIRST AND (B) SECOND HARMONICS.

5. ACOUSTIC FEEDBACK?

The evidence laid out so far appears to point towards a resonance mechanism that occurs primarily for this blade trailing edge thickness (CMC-9, the largest of the set), turbulence intensity (higher value between the runs, at ~13%) and only a certain Reynolds number range. Given the Reynolds number range is fairly narrow, we consider the possibility that this may be an acoustic feedback based on the geometrical parameters of the blade cascade and their interaction with the frequencies related to vortex shedding.

The vortex shedding frequency of the trailing edge can be compared to the more well-understood case of a round cylinder. For the cylinder, there are several regimes depending on the Reynolds number. For example, the measurements by Achenbach and Heinecke [23] of the smooth cylinder indicate a critical transition at $Re_{D,cr} = 3 \times 10^6$, where the shedding frequency switches from the subcritical $St_D \sim 0.22$ to the transcritical $St_D \sim 0.5$. The transitions occur when significant changes to the boundary layer occur, such as the formation of separation bubbles or movement of the separation point [24]. We observe that the shedding fundamental frequency seems to normalize to a Strouhal number of $St_{D_{TE}} \sim 0.21 - 0.22$ as displayed in Figure 10 (a), matching what would be a subcritical shedding condition of the circular cylinder. Slight changes in shedding frequency as shown in Figure 10 are also observed in circular cylinders and are linked to a continuous evolution of the conditions of the boundary layer as the Reynolds number increases.

From Figure 10, we also glean what perhaps is a clue for why certain Reynolds numbers seem to form a resonant loop whereas other Reynolds numbers do not. We can note that clearly there is an upwards trend on the frequency of the vortex shedding as a function of Reynolds number for both the first and second harmonics, with an increase in frequency of about 5%. It appears this trend is in contrast with Sieverding and Heinemann's measurements [25], which display an opposing trend as a function of Reynolds number. We believe this is related to the normalization used by the reference, which includes the boundary layer thicknesses, whereas we do not. This trend of shift in the physical frequency of the shedding, however, opens the possibility to a phase-locking mechanism based on the geometrical characteristics of the blade configuration. More specifically, if there is communication between different regions of the flow that can cause a resonance-like mechanism, then the arrival phase of the disturbance produced at one location must be correct to excite a new disturbance at a separate location such that it will interfere constructively with the oscillations occurring at a second location in the flow. As the shedding Strouhal number is a weak function of Reynolds number for the thick turbine blades (as also observed in circular cylinders), the timing conditions for resonance may only be fulfilled at certain Reynolds numbers because those produce the correct shedding Strouhal number. We also note, for context, that although we do not currently have boundary layer measurements, we observe in the LES simulations of Miki et al. [4] that a change in the suction trailing edge boundary layer profile appears to occur for the high-loss regime. We are unable to detect the shape of the boundary layer through our images, but we observe all conditions appear to have a certain degree of texture in the schlieren images near the suction wall, indicating some degree of turbulence still remains in the boundary layers.

There are multiple potential feedback mechanisms available involving the acoustic waves produced at the trailing edge that could enhance the vortex shedding. In Figure 11 we consider a few possible cases as a non-exhaustive list of potential mechanisms involving a upstream-directed acoustic wave and downstream-directed acoustic/fluidic disturbance. We'll refer to these mechanisms as either "cascading" for paths that do not form a loop but can amplify over several blades; or "resonant" to refer to paths that are a closed-loop interaction within a single blade or a blade pair. For example, the downwards-running acoustic wave (1) in Figure 11 (a) could provide a non-resonant, cascading path for disturbance magnification where the upper blades in this coordinate system produce acoustic waves that cause the lower blades to experience an excitation that, if in phase with the preexisting shedding, can cause magnified shedding and over several

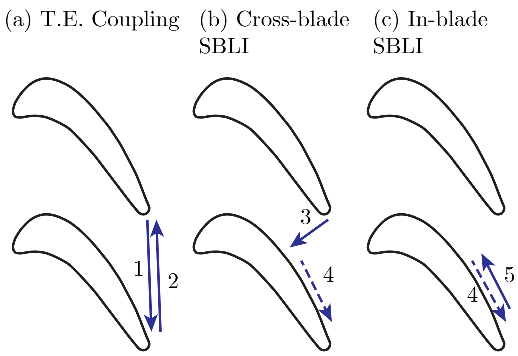

FIGURE 11: VIABLE FEEDBACK MECHANISMS FOR ACOUSTIC EXCITATION OF THE BLADE TRAILING EDGE VORTEX SHEDDING. SOLID LINES ARE ACOUSTIC WAVE PROPAGATION, WHEREAS DASHED LINES ARE INSTABILITY WAVE PROPAGATION WITHIN THE BOUNDARY LAYER.

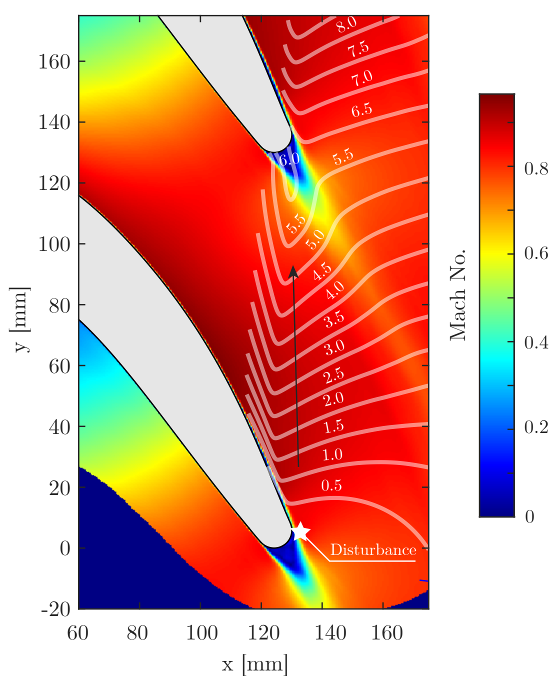

FIGURE 12: WAVES PROPAGATED UPSTREAM AGAINST THE MEAN FLOW FROM A DISTURBANCE LOCATED AT THE TRAILING EDGE, BASED ON LES DATA [4]. WHITE TRANSPARENT SOLID LINES: ACOUSTIC WAVES. NUMBERS ON CONTOURS: NUMBER OF CYCLES OF THE FUNDAMENTAL AT 4375 HZ ELAPSED FROM THE DISTURBANCE.

cascades can gather sufficient amplitude for transonic shock formation. Similarly, the upwards-running acoustic wave (2) can also provide a cascading path where the lower blades excite the upper blades. These two paths shown in Figure 11 (a) can also be combined as a resonant mechanism; i.e., the wave (1) travels to the lower blade and is reflected after some phase delay returning as a wave (2) back to the upper blade as a resonant feedback loop.

Another possibility is the involvement of the boundary layer as a feedback amplification mechanism, as suggested by Miki et al. [4]. For example, Figure 11 (b) illustrates a cascading amplification mechanism where the acoustic wave (3) produced by the upper blade trailing edge rollup interacts with the boundary layer at the suction side of the lower blade, which is already experiencing an adverse pressure gradient and may be prone to amplification of disturbances. The disturbance then advects through the boundary layer with the flow (4), growing in amplitude. If the disturbance arrives at the trailing edge with the correct phase, it will cause enhancement of the vortex shedding of the lower blade, causing a cascading amplification over a few blades. Similarly, this mechanism also could be resonant if a feedback path is established through the acoustic wave (1).

Finally, another resonant feedback mechanism to consider is displayed in Figure 11 (c), where an acoustic wave produced by any blade trailing edge travels upstream through the boundary layer, disturbing it along the way in its entirety. The effect of the acoustic wave is then amplified and travels downstream with multiple different time delays, and certain disturbances will arrive with the correct phase to further excite the vortex shedding. In this case, resonance is guaranteed unless the loop gain is lower than unity at certain conditions.

Although it is not possible to test the hypothesis of the feedback loop described in Figure 11 (c) through a simple timing analysis with the data we acquired so far, the four mechanisms described in Figure 11 (a) and (b) can be tested by using the mean velocity and acoustic field coming from a simulation of this flow. These are the possible mechanisms we can consider in a timing analysis: (path 1) is the T.E. coupling, downstream-running; (path 2) is the T.E. coupling, upstream-running; (paths 1+2) is the T.E. coupling, resonant; whereas (b) is the cross-blade SBLI mechanism, which can be cascading (paths 3+4) or resonant (paths 3+4+2).

First, a view of the feedback path (2) is considered by placing a disturbance point close to the top shear layer of the bottom blade as shown in Figure 12, which is built by propagating an acoustic wave from the disturbance location shown by using the average velocity field obtained through the LES simulation result [4]. The disturbance travels at the acoustic wave speed, upstream, being distorted by the local velocity gradients. The white transparent lines shown in Figure 12 represent the integer and half-integer multiples of the 4375 Hz wave, which corresponds to the SPOD peak at $Re/Re_b = 1.00$. This wave by itself represents the upstream-running cascading mechanism, and is part of the other two resonant loops described previously. Note in Figure 12 that the wave propagates through the boundary layer faster than against the stream between the blades, becoming a heavily distorted wavefront. The distorted wavefront, however, focuses around the trailing edge of the upper blade at approximately 6.0 cycles of the first harmonic of the trailing edge shedding frequency, forming a caustic wave that embraces around the two shear layers and focuses in the middle of the fluid - potentially enhancing a disturbance that could occur in that location. The timing analysis shows that the waves arrive with an integer number of cycles in the $Re/Re_b = 1.00$ condition, making this path a viable mechanism for resonant or cascading feedback.

Looking at the downstream-running acoustic wave produced by a disturbance produced at the top blade trailing edge, as

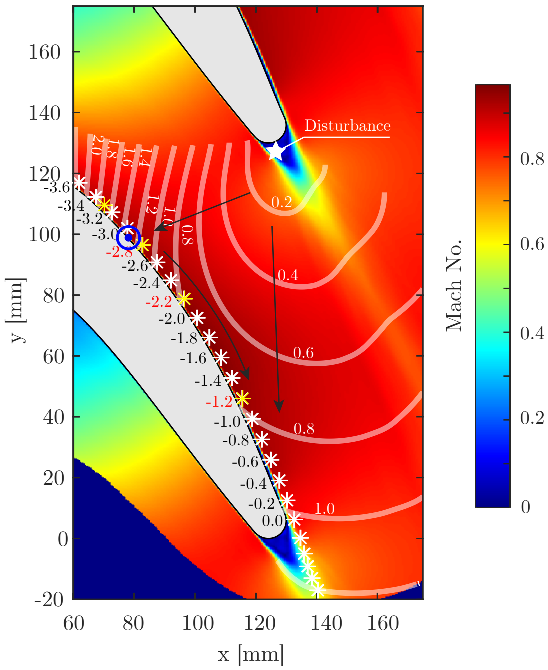

FIGURE 13: WAVES PROPAGATED DOWNSTREAM WITH THE MEAN FLOW FROM A DISTURBANCE LOCATED AT THE TRAILING EDGE, BASED ON LES DATA [4]. WHITE TRANSPARENT SOLID LINES: ACOUSTIC WAVES. WHITE STARS: INSTABILITY WAVES ADVECTED AT 0.6$\vec{u}$. NUMBERS ON CONTOURS OR STARS: NUMBER OF CYCLES OF THE FUNDAMENTAL ELAPSED FROM THE DISTURBANCE. YELLOW STARS: APPROXIMATE POSITIONS WHERE AN INTEGER NUMBER OF CYCLES ELAPSES FROM THE UPSTREAM BLADE ACOUSTIC WAVE TO THE DOWNSTREAM BLADE TRAILING EDGE. BLUE ⊙: POSITION OF TAP #27 LOCATED AT THE GEOMETRIC THROAT.

displayed in Figure 13, we observe several potential feedback mechanisms that together could contribute to the resonance phenomenon only at a certain Reynolds number range. First, we direct the reader's attention to the downstream-running wave propagating freely in the space between the two trailing edges. The numbered transparent white lines display that the time it takes for a wave to propagate from the trailing edge of the upstream blade to the trailing edge of the downstream blade (path 1 in Figure 11) is very close to a single cycle of the first harmonic of the shedding frequency. This means the upstream-downstream resonant mechanism (path 1+2 in Figure 11) is viable for this blade configuration, as roundtrip time is an integer number of shedding cycles.

On the other hand, Figure 13 also reveals that the SBLI mechanism may also be viable. We now direct the readers' attention to the asterisks drawn over the suction surface of the downstream blade. The asterisks are integrated in the streamwise direction by using 60% of local mean velocity just outside of the boundary layer, based on a typical convective velocity of near-wall pressure disturbances [26, 27]. This velocity would represent the convection velocity of a boundary layer disturbance; although the actual velocity may vary from this number depending on its wavenumber and frequency. The asterisks, which are evenly spaced at 0.2 times the shedding frequency cycle, are numbered backwards from the trailing edge of the bottom blade. As can be seen in Figure 13, there are certain locations where the disturbance emanating from the upstream blade's trailing edge, when added to the convected disturbance, will complete an integer number of cycles to reach the downstream blade's trailing edge. These locations are highlighted in red text along with yellow asterisks. There are four locations of interest, at {-1.2, -2.2, -2.8, -3.3} cycles from the trailing edge. All these locations will synchronize the trailing edges of the top and bottom blade through a downstream-advecting boundary layer communication path.

The blade loading data captured in a previous campaign (not presented herein) shows that certain locations on the suction side of the blade had a much lower absolute value for the suction peak at the high-loss TVS Reynolds numbers, especially near the geometric throat of the blade cascade. The location of the most affected pressure port is, in fact, at the geometric throat (tap #27), provided as a blue ⊙ symbol in Figure 13. Note this location coincides very closely to the {-2.8} cycles from the trailing edge, which is one of the viable candidates for an integer feedback mechanism. This is noteworthy, as it may indicate a very strong candidate feedback path as the (3+4+2) path: A pressure fluctuation produced at the top blade trailing edge due to regular vortex shedding will travel acoustically through the fluid and interact with the suction surface of the bottom blade, creating a strong disturbance at the suction side boundary layer. This disturbance travels along with the boundary layer, potentially growing exponentially into a large amplitude wavepacket. When the disturbance reaches the trailing edge of the bottom blade 4 cycles after the initial disturbance was generated, it produces a stronger acoustic wave as the trailing edge vortex rolls up on the bottom blade shear layer. That wave propagates upstream as another acoustic wave, reaching the upper blade trailing edge 10 cycles after the initial disturbance was produced. After multiple cycles in steady-state operation, it is not unreasonable to imagine that a lock-in of the phases can happen with the right conditions in place.

Finally, we add that the in-blade mechanism outlined in Miki et al. [4] involving the paths (4) and (5) in Figure 11 is also not ruled out through this timing analysis, since the upstream/downstream paths can always form integer numbers of cycles at many different positions in the suction side, requiring no timing analysis because the lock-in is guaranteed. However, it is unclear why only a narrow range of shedding frequencies would support an enhancement of the vortex shedding process. A path forward to clarify and further determine the physics behind these mechanisms is to explore the effect of changing the fundamental shedding frequency while keeping the other problem variables constant, which could be accomplished by performing small changes to the trailing edge thickness that would affect the physical shedding frequency enough to disturb the feedback loop at the current resonant Reynolds number of $Re/Re_b = 0.87$.

6. CONCLUSION

Our observations from a high-speed self-aligned focusing schlieren test campaign performed on the CMC-9 turbine cascade at NASA GRC point to rich physics that arise potentially from a resonance mechanism involving the acoustic or shock waves propagating within the space between the blades. Our SPOD analysis facilitated the evaluation and summarization of the amplitude and frequency observed from the complex shock train images, enabling the detection of the shedding frequency trend as a function of Reynolds number and establishing that acoustic wave production related to the trailing edge vortex shedding is present in all conditions. The shedding frequency, however, varies by about 6% over the Reynolds number range tested (spanning a factor of 6), which points to the possibility for phase-locking mechanisms of the waves produced within the flow that can enable the production of very high amplitude waves. We considered a few feedback paths through a timing analysis based on the mean LES fields from a companion simulation, and identified that the shocks produced at one blade's trailing edge are likely interacting with the boundary layer at the suction side of the neighboring blade at the correct timing and location to cause a convective boundary layer disturbance to constructively interfere with the trailing edge vortex formation. This mechanism, along with the in-blade SBLI mechanism involving a single blade, appear to be the most likely candidates to explain the enhanced TVS observed over the Reynolds number range tested.

ACKNOWLEDGMENTS

This work was supported by the NASA Subsonic Vehicle Technologies and Tools Project. The first author was supported by the NASA Glenn Faculty Fellowship program at the NASA Glenn Research Center.

REFERENCES

[1] Boyle, Robert, Halbig, Michael, Parikh, Ankur and Nagpal, Vinod. "Design Considerations for Ceramic Matrix Composite Vanes for High Pressure Turbine Applications." *Proceedings of the ASME Turbo Expo 2013*. GT2013-95104. San Antonio, Texas, June 3–7, 2013.

[2] Sieverding, Claus and Manna, Marcello. "A Review on Turbine Trailing Edge Flow." *International Journal of Turbomachinery, Propulsion and Power* Vol. 5 No. 2 (2020). DOI 10.3390/ijtpp5020010.

[3] Giel, Paul, Shyam, Vikram, Juangphanich, Paht and Clark, John P. "Effects of Trailing Edge Thickness and Blade Loading Distribution on the Aerodynamic Performance of Simulated CMC Turbine Blades." *Proceedings of the ASME Turbo Expo 2020*. GT2020-15802. London, England, June 22–26, 2020. DOI 10.1115/GT2020-15802.

[4] Miki, Kenji, Ameri, Ali and Giel, Paul. "Large Eddy Simulation Analysis of Loss Anomaly of a Turbine Blade With Large Trailing Edge Radius." *Journal of Turbomachinery* Vol. 147 No. 3 (2024): p. 031012. DOI 10.1115/1.4066914. URL https://doi.org/10.1115/1.4066914.

[5] Melzer, A. P. and Pullan, G. "The Role of Vortex Shedding in the Trailing Edge Loss of Transonic Turbine Blades." *Journal of Turbomachinery* Vol. 141 No. 4 (2019): p. 041001. DOI 10.1115/1.4041307.

[6] *Shock Wave-Boundary-Layer Interactions*. Cambridge Aerospace Series, Cambridge University Press (2011).

[7] Rossiter, A. D., Pullan, G. and Melzer, A. P. "The Influence of Boundary Layer State and Trailing Edge Wedge Angle on the Aerodynamic Performance of Transonic Turbine Blades." *Journal of Turbomachinery* Vol. 145 No. 4 (2022): p. 041008.

[8] Rossiter, A. D. "Trailing Edge Aerodynamics: Flow Regimes, Geometry and Loss." PhD thesis, University of Cambridge. 2023. DOI 10.17863/CAM.100240.

[9] McVetta, Ashlie, Giel, Paul and Welch, Gerard. *Aerodynamic Investigation of Incidence Angle Effects in a Large Scale Transonic Turbine Cascade* (2012): DOI 10.2514/6.2012-3879. URL https://arc.aiaa.org/doi/abs/10.2514/6.2012-3879.

[10] Giel, Paul W., Boyle, Robert J. and Bunker, Ronald S. "Measurements and Predictions of Heat Transfer on Rotor Blades in a Transonic Turbine Cascade." *Journal of Turbomachinery* Vol. 126 No. 1 (2004): pp. 110–121. DOI 10.1115/1.1643383. URL https://doi.org/10.1115/1.1643383.

[11] Flegel, Ashlie B., Giel, Paul W. and Welch, Gerard E. *Aerodynamic Effects of High Turbulence Intensity on a Variable-Speed Power-Turbine Blade with Large Incidence and Reynolds Number Variations* (2014): DOI 10.2514/6.2014-3933. URL https://arc.aiaa.org/doi/abs/10.2514/6.2014-3933.

[12] Thurman, Doug, Flegel, Ashlie B. and Giel, Paul W. *Inlet Turbulence and Length Scale Measurements in a Large Scale Transonic Turbine Cascade* (2014): DOI 10.2514/6.2014-3934. URL https://arc.aiaa.org/doi/abs/10.2514/6.2014-3934.

[13] Bathel, Brett F. and Weisberger, Joshua M. *Development of a Self-Aligned Compact Focusing Schlieren System for NASA Test Facilities* (2022): DOI 10.2514/6.2022-0560. URL https://arc.aiaa.org/doi/abs/10.2514/6.2022-0560.

[14] Page, Wayne E., Boyda, Matthew T., Fahringer, Timothy W., Weisberger, Joshua M., Bathel, Brett F., Wernet, Mark and Heineck, James T. *Recent Progress and Development of Self-Aligned Focusing Schlieren* (2025): DOI 10.2514/6.2025-1061. URL https://arc.aiaa.org/doi/abs/10.2514/6.2025-1061.

[15] Steinthorsson, E., Liou, M.-S. and Povinelli, L.A. *Development of an explicit multiblock/multigrid flow solver for viscous flows in complex geometries* (1993): DOI 10.2514/6.1993-2380. URL https://arc.aiaa.org/doi/abs/10.2514/6.1993-2380.

[16] Bryanston-Cross, P. J. and Camus, J. J. "Auto and Cross-Correlation Measurements in a Turbine Cascade Using a Digital Correlator." *Proceedings of the ASME 1982 International Gas Turbine Conference and Exhibit*. 82-GT-132. London, England, April 18–22, 1982. URL https://asmedigitalcollection.asme.org/GT/proceedings-pdf/GT1982/79566/V001T01A055/2394140/v001t01a055-82-gt-132.pdf.

[17] Towne, Aaron, Schmidt, Oliver T. and Colonius, Tim. "Spectral proper orthogonal decomposition and its relationship to dynamic mode decomposition and resolvent analysis." *Journal of Fluid Mechanics* Vol. 847 (2018): p. 821–867. DOI 10.1017/jfm.2018.283.

[18] Sieber, Moritz, Paschereit, C. Oliver and Oberleithner, Kilian. "Spectral proper orthogonal decomposition." *Journal of Fluid Mechanics* Vol. 792 (2016): p. 798–828. DOI 10.1017/jfm.2016.103.

[19] Arndt, R. E. A., Long, D. F. and Glauser, M. N. "The proper orthogonal decomposition of pressure fluctuations surrounding a turbulent jet." *Journal of Fluid Mechanics* Vol. 340 (1997): p. 1–33. DOI 10.1017/S0022112097005089.

[20] Delville, J., Ukeiley, L., Cordier, L., Bonnet, J. P. and Glauser, M. "Examination of large-scale structures in a turbulent plane mixing layer. Part 1. Proper orthogonal decomposition." *Journal of Fluid Mechanics* Vol. 391 (1999): p. 91–122. DOI 10.1017/S0022112099005200.

[21] Schmidt, Oliver T. and Colonius, Tim. "Guide to Spectral Proper Orthogonal Decomposition." *AIAA Journal* Vol. 58 No. 3 (2020): pp. 1023–1033. DOI 10.2514/1.J058809.

[22] Blackstock, David T. *Fundamentals of Physical Acoustics*. Wiley-Interscience, New York (2000).

[23] Achenbach, E. and Heinecke, E. "On vortex shedding from smooth and rough cylinders in the range of Reynolds numbers 6E3 to 5E6." *Journal of Fluid Mechanics* Vol. 109 (1981): p. 239–251. DOI 10.1017/S002211208100102X.

[24] Capone, Alessandro, Klein, Christian, Di Felice, Fabio and Miozzi, Massimo. "Phenomenology of a flow around a circular cylinder at sub-critical and critical Reynolds numbers." *Physics of Fluids* Vol. 28 No. 7 (2016): p. 074101. DOI 10.1063/1.4954655.

[25] Sieverding, C. H. and Heinemann, H. "The Influence of Boundary Layer State on Vortex Shedding from Flat Plates and Turbine Cascades." *Proceedings of the ASME 1989 International Gas Turbine and Aeroengine Congress and Exposition*. 89-GT-296. Toronto, Canada, June 4-–8, 1989. URL https://asmedigitalcollection.asme.org/turbomachinery/article/112/2/181/434233/The-Influence-of-Boundary-Layer-State-on-Vortex.

[26] Kim, John and Hussain, Fazle. "Propagation velocity of perturbations in turbulent channel flow." *Physics of Fluids A: Fluid Dynamics* Vol. 5 No. 3 (1993): pp. 695–706. DOI 10.1063/1.858653.

[27] Del Alamo, Juan C. and Jimenez, Javier. "Estimation of turbulent convection velocities and corrections to Taylor's approximation." *Journal of Fluid Mechanics* Vol. 640 (2009): p. 5–26. DOI 10.1017/S0022112009991029.